



## Shape control and design of aeronautical configurations using shape memory alloy actuators

Nikolaos Simiriotis, Michalis Fragiadakis, Jean-François Rouchon, Marianna Braza

### ► To cite this version:

Nikolaos Simiriotis, Michalis Fragiadakis, Jean-François Rouchon, Marianna Braza. Shape control and design of aeronautical configurations using shape memory alloy actuators. *Computers & Structures*, 2021, 244, pp.106434. 10.1016/j.compstruc.2020.106434 . hal-03101488

**HAL Id: hal-03101488**

**<https://hal.science/hal-03101488>**

Submitted on 7 Jan 2021

**HAL** is a multi-disciplinary open access archive for the deposit and dissemination of scientific research documents, whether they are published or not. The documents may come from teaching and research institutions in France or abroad, or from public or private research centers.

L'archive ouverte pluridisciplinaire **HAL**, est destinée au dépôt et à la diffusion de documents scientifiques de niveau recherche, publiés ou non, émanant des établissements d'enseignement et de recherche français ou étrangers, des laboratoires publics ou privés.



## Open Archive Toulouse Archive Ouverte

OATAO is an open access repository that collects the work of Toulouse researchers and makes it freely available over the web where possible

This is an author's version published in: <https://oatao.univ-toulouse.fr/27221>

### Official URL:

<https://doi.org/10.1016/j.compstruc.2020.106434>

### To cite this version:

Simiriotis, Nikolaos and Fragiadakis, Michalis and Rouchon, Jean-François and Braza, Marianna *Shape control and design of aeronautical configurations using shape memory alloy actuators*. (2021) Computers & Structures, 244. 106434. ISSN 0045-7949

Any correspondence concerning this service should be sent to the repository administrator: [tech-oatao@listes-diff.inp-toulouse.fr](mailto:tech-oatao@listes-diff.inp-toulouse.fr)

# Shape control and design of aeronautical configurations using shape memory alloy actuators

N. Simiriotis<sup>a,\*</sup>, M. Fragiadakis<sup>b</sup>, J.F. Rouchon<sup>c</sup>, M. Braza<sup>a</sup>

<sup>a</sup>Institut de Mécanique des Fluides de Toulouse (IMFT), UMR 5502 CNRS-INPT-UPS, 2 Allée du Professeur Camille Soula, 31400 Toulouse, France

<sup>b</sup>National Technical University of Athens (NTUA), 9 Iroon Polytechniou 15780, Zografou Campus, Athens, Greece

<sup>c</sup>Laboratoire Plasma et Conversion d'Energie (LAPLACE), UMR 5213 CNRS-INPT, 2 rue Charles Camichel, 31071 Toulouse, France

## Keywords:

SMA  
Smart materials  
Morphing  
Shape control  
Optimization  
Aeronautics

The paper proposes an efficient methodology that allows to design smart deformable aeronautical configurations that are able to achieve pre defined target shapes by adjusting the temperature of Shape Memory Alloy (SMA) actuators. SMA based actuation finds extensive application in *morphing* concepts which are adopted in aeronautics to enhance the aerodynamic performance by continuously varying the geometry of the wing. A novel robust algorithm, developed for predicting the nonlinear response of the SMA structure interaction problem is presented. The algorithm is coupled with an optimization method in order to predict the optimal structural and operational parameters with respect to target shapes of the controlled configuration. The design methodology presented in this study selects the design parameters of the problem at hand, i.e. the location of the actuators and the operating temperature, for given loading conditions. The proposed methodology is validated and demonstrated with three case studies, including the design of a real world aeronautical configuration.

## 1. Introduction

Morphing of aeronautical configurations is the efficient multi point shape adaptability of a deformable structure [1]. In the context of disruptive aircraft configurations, the wing shape is optimized in order to enhance the aerodynamic performance. Ideally, the morphing wings should be flexible enough and able to deform continuously in order to adapt to the different flight stages. At the same time, the morphing structure should be able to sustain the large aerodynamic loads imposed by the flight conditions [2]. Past morphing concepts were associated with increased complexity, sizing issues and weight penalties, especially for distributed actuating systems, i.e. configurations with multiple actuators that should be fitted in a limited space [3]. These limitations almost overshadow the aerodynamic benefits and have prevented morphing to be implemented in aeronautics for many years. However, as smart materials are finding more and more applications in practice, the use of Shape Memory Alloys (SMA) allows reconsidering morphing as one of the main solutions to overcome the levelling of the

aircraft performance and many of the drawbacks of previously developed morphing architectures.

SMAs are alloys that transform thermal energy into mechanical stress. Therefore, by positioning pairs of SMA actuators within the structure, it is possible to apply large forces and modify its shape by adjusting the temperature of every actuator. Since the energy transformation occurs due to the intrinsic properties of the material [2], the SMA actuators can be used for constructing safer and lighter systems of reduced complexity, and compatible with the future electric aircraft concept. Structural applications of SMAs in almost every field of engineering are discussed extensively in [4]. One of the first works that studied numerically the SMA structure interaction problem is the that of Brinson et al. [5]: they present a nonlinear beam formulation coupled with an SMA actuator. The problem was also addressed in [6] using a different SMA constitutive model. Both studies attempted to demonstrate the control efficiency of SMAs and the predictive capabilities of the constitutive models used, but are limited to simple academic examples. The coupling with a finite element (FE) code for solving more complicated geometries was discussed in [7] where the SMA actuators were modeled as adaptive trusses and a solution procedure was implemented into a commercial software code. Furthermore, Ref. [8] also adopted FE simulations and focused on designing SMA hybrid composites that can be actuated and adaptively stiffen or change their shape.

The aforementioned studies solve the structure SMA interaction problem without examining the use of SMA actuators for shape control applications. One of the first works in this direction, is that of Barbarino et al. [9] who presented numerical results for the morphing of a trailing edge in which the displacement is controlled using SMA based actuation. Experimental and numerical studies were also carried out in [10] for the design of a flap architecture with a variable camber trailing edge. The authors considered the reference geometry of a full scale wing of a regional aircraft and their approach took into account the SMA properties, the aerodynamic loading and the response of the wing. Furthermore, a preliminary design study with FE simulations was presented by Icardi and Ferrero [11] for the adaptive wing of a small unmanned air vehicle (UAV), totally driven by SMA devices. The authors verified that the wing can sustain the aerodynamic pressure under different flight conditions, without any weight increase or stiffness loss compared to other conventional actuators. Solomou et al. [12] developed a beam element that incorporates the thermo mechanical properties of SMA wire actuators. The study of [13] followed these developments, coupled the FE model with a lower fidelity fluid solver and performed a fluid structure interaction (FSI) study for a hinged flap configuration and a segmented airfoil, targeting wind turbine applications.

The above mentioned studies focus on the development of solution strategies for the numerical prediction of the static/dynamic response of morphing aeronautical configurations. However, they do not explicitly propose a method for the optimal design of configurations that are able to achieve a target shape. Model based methods for the optimal control of smart structures are extensively examined in the review paper of Seelecke and Müller [14]: they discuss various aspects of modeling and optimal feedback control methods that account for the nonlinear hysteretic behavior of SMAs. Experimental and numerical studies in [15] aimed to optimize the offset distance used in controlling a simple flexible beam. Ameduri et al. [16] also optimized an SMA system to be integrated within a morphing flap. The authors performed detailed parametric studies and a heuristic optimization procedure using a simplified model. A deterministic global optimization of the flapping kinematics of a morphing wing was carried out by Ghommem et al. [17]: they focused on parametrizing the morphing deformation to produce reduced order models and optimizing the controlled response with respect to the propulsive efficiency. However, the above studies are problem specific and it is difficult to adopt the proposed formulations in systems of higher complexity.

Until today, none of the past developments on SMA based systems have led to a concept integrated to a real aircraft. This is due to the fact that the design procedure for an SMA based actuation system is hampered by conflicting requirements that should be met. More specifically, in order to control large scale aeronautical structures, the number of actuators that must fit in a limited space significantly increases. This increases the material and operational costs, adds weight and affects the size of the actuation system. Therefore, it is important to develop numerical tools for the design of SMA based morphing aeronautical configurations.

To address this issue, the aim of the present study is to propose a design methodology for “smart” morphing wings that are able to obtain pre described shapes during different flight phases using SMA actuators. The proposed approach consists of two steps: (a) a robust algorithm that solves the *coupled structure SMA* problem in the context of a FE analysis software, and (b) the coupling of the whole procedure with an optimization method in order to find configurations able to attain target shapes using SMA actuators. In the present approach, the structure is modeled with the FE method which allows integrating the various components included in a complex aeronautical structure. The thermomechanical behavior

of SMA actuators is coupled with the deformable configuration to calculate the internal stresses due the heating/cooling of the actuator. The optimization phase is introduced in order to determine the specific design variables and to create architectures able to reach desired shapes. The methodology takes into account the structural specifications, the imposed external loading conditions, geometric (e.g. limited space) and/or the operational constraints (e.g. maximum power supply). The algorithm presented in this study can produce optimal morphing configurations and simple/robust designs. The latter is an important aspect for safety characterization and certification. Furthermore, constraints on the actuation temperature can produce “greener” architectures, in terms of power consumption.

The work presented is part of the H2020 European research project “Smart Morphing & Sensing (SMS) for Aeronautical configurations” [18], where *hybrid*, partly bio inspired, electroactive morphing concepts are investigated. In the hybrid concept, different classes of electroactive actuators are employed to increase the lift to drag ratio and simultaneously reduce the aerodynamic noise. In this project, SMA actuators were included in the construction of an electroactive hybrid Morphing Wing Prototype (MWP) ([19,20]).

## 2. Thermo-mechanical behavior of SMA materials

The thermo mechanical behavior of SMA materials is already well documented, e.g. [21,4], and it is here briefly summarized for the sake of completeness in order to introduce the parameters and the assumptions adopted in this work. SMAs are quite efficient since they have high maximum stress capacity (around 350 MPa for Nickel Titanium compounds) and they can recover from large strain (ranging between 6% and 10%). SMAs are found in two states: the austenite phase and the martensite phase. The martensite phase can be either twinned or detwinned, depending on the stress conditions. The state of the material depends on its temperature and on the applied mechanical load. In a *stress free* state, SMAs are characterized by four phase changing temperatures:  $A_s, A_f$  which control the start and the end of the austenitic transformation respectively, and  $M_s, M_f$  for the martensitic transformation. For the materials considered in this article, the phase changing temperatures are always  $M_f < M_s < A_s < A_f$ . For temperatures between  $M_f$  and  $A_s$ , no phase changes take place and the material is either in an austenite or in a martensite phase. Austenite phase is characterized by *pseudo elasticity*, which refers to the non existence of residual strains after a cycle of loading and unloading at a temperature higher than  $A_f$ . The *shape memory effect* is linked to the recovery of large residual strains of multi variant (i.e. twinned or detwinned) martensite. After being turned into single variant martensite, due to the application of stress, the SMA has to be heated at a temperature beyond  $A_f$  for the residual strain to be fully recovered.

Based on the properties described above, the working principle of an SMA based actuation can be understood by looking at the simple demonstration shown in Fig. 2. An SMA strut, with initial length  $L$ , is elongated by  $\Delta L$  at a temperature  $T_0 < M_f$  in order to be attached to an undeformed spring. The deformation of the SMA strut produces a detwinned martensitic fraction within the material. Once heated at a temperature  $T_1 > A_f$ , an austenitic transformation takes place and the SMA strut recovers its initial undeformed shape  $L$ . When the strut is cooled down back to  $T_0$ , the martensitic fraction redevelops due to the stress condition imposed from the spring connected to the SMA strut. In the general case, the final equilibrium point differs from the first equilibrium point that was imposed after the prestrain of the strut.

In order to account for the thermomechanical SMA properties and numerically predict the structural response of a controlled configuration, a number of constitutive relationships have been proposed in the literature. Phenomenological models relate stress, strain and martensite fraction through a law that governs the martensitic transformation as a function of temperature and stress. These type of models are both robust and easily incorporated into a FE software producing sufficiently accurate results for the applications examined. One dimensional models are able to account for every significant feature of the SMA thermomechanical behavior [4]. They have a simple formulation and rely on a small number of material parameters. Various uniaxial material models for SMAs have been proposed by different research groups. They can be divided in three families: (a) those based on the Tanaka model [22] (e.g. Liang Rogers [23], Brinson [24]), (b) models based on the work of Auricchio and his coworkers [25,26], and (c) models based on the work of Lagoudas and his co workers [27]. The Brinson model (Fig. 1) is adopted in the present study. This Tanaka based model is an extension of the Liang Rogers model that accounts for multi variant martensite.

All of the Tanaka based models utilize the same well known constitutive equation that couples the mechanical stress, the thermo plastic stress and the stress due to the phase transformation:

$$\sigma = \sigma_0 + E(\xi)(\epsilon - \epsilon_0) + \Theta(T - T_0) + \Omega(\xi)(\xi - \xi_0) \quad (1)$$

where  $\sigma$  is the uniaxial mechanical stress,  $\epsilon$  is the reduced strain,  $T$  is the temperature,  $E$  is the modulus of elasticity, while  $\Theta$  and  $\Omega$  are the thermal elasticity measure and the phase change factor, respectively.  $\Theta$  and  $\Omega$  are material characteristics that are measured experimentally at a zero stress state. The subscript "0" refers to quantities in their initial state, while  $T_0$  is the temperature for which the thermal strain is zero. The non dimensional quantity  $\xi(\sigma, T)$  expresses the martensitic fraction of the material, i.e. when  $\xi = 1$  the material is in a full martensitic state and when  $\xi = 0$  the material is austenitic. Both the elastic modulus and the phase change coefficient are functions of  $\xi$ :

$$E(\xi) = E_A + (E_M - E_A)\xi, \quad \Omega(\xi) = \epsilon_L E(\xi) \quad (2)$$

where  $\epsilon_L$  is the maximum residual strain which is assumed constant for the whole range of temperatures below  $A_f$ .  $E_A$  is the austenitic and  $E_M$  the martensitic modulus of elasticity. In [24], it is shown that Eq. 1 can be simplified to:

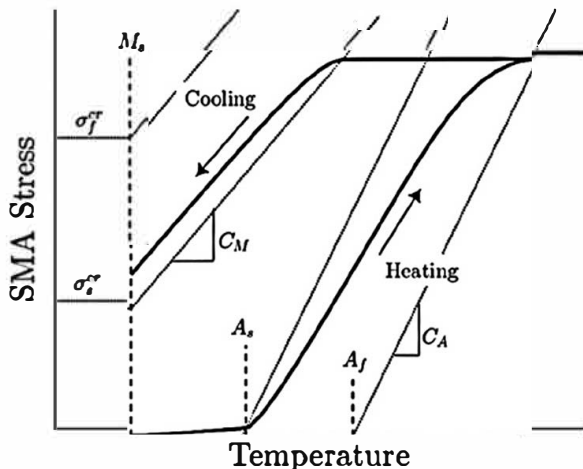


Fig. 1. Stress-temperature diagram as modeled by Brinson: austenite to detwinned martensite conversion for  $T > M_s$  and  $\sigma_f^T + C_M(T - M_s) < \sigma < \sigma_f^T + C_M(T - M_s)$ ; twinned to detwinned martensite conversion for  $T < M_s$  and  $\sigma_f^T < \sigma < \sigma_f^T$ ; martensite to austenite conversion for  $T > A_s$  and  $C_A(T - A_f) < \sigma < C_A(T - A_s)$ .

$$\sigma = E(\xi)(\epsilon - \epsilon_L \xi_s) + \Theta(T - T_0) \quad (3)$$

after introducing a separation of the volume fraction:  $\xi = \xi_T + \xi_s$ . The parameter  $\xi_T$  accounts for the temperature induced martensite, while  $\xi_s$  accounts for the stress induced percentage. Consequently, the model is able to account for the detwinning of the martensite that is responsible for the shape memory effect at lower temperatures. The transformation equations are modified to accommodate this separation of the volume fraction. Below the temperature  $M_s$ , critical stress limits  $\sigma_s^T$  and  $\sigma_f^T$  apply, guiding the conversion between martensite variants. For higher temperatures, the stress influence coefficients  $C_M$  and  $C_A$  express the dependence of the transformation temperature on the stress. The transformation equations can be found in [24] and the thermomechanical behavior of the model is presented in Fig. 1. Since the phase change equations contain cosine functions, their arguments are constrained so that a phase change occurs when both the temperature and the stress ranges are within the proper transformation regions. Finally, the modification of the martensite transformation law developed by Chung et al. [28] is adopted in this work.

### 3. Structural shape control using SMA actuators

During different flight phases, different wing shapes are required. Wing morphing using SMA actuators relies on the active control of the aerodynamic shape so that the controlled structure is able to achieve one, or more, pre described target shapes. The shape control refers to the identification of equilibrium points between the deformation capacity of the structure and the extension capacity of the SMA actuator which is a function of the thermomechanical properties of the material. The solution requires the coupling of the nonlinear thermomechanical behavior law of the SMA with the structure's response to any temperature change of the actuators. The coupling is accomplished through an iterative procedure since the complete system is material nonlinear due to the SMA actuators and geometrically nonlinear due to the large displacements that the morphing structure typically undergoes.

A possible morphing concept is shown in Fig. 3. The airfoil is cambered with the aid of SMA actuators placed on the ribs/platelets that are connected using hinges in order to maximize the deformation capacity of the structure. The SMA actuators, acting as "tendons", provide the torque necessary to rotate the ribs/platelets in order to adjust the aerodynamic shape. The SMAs are positioned in pairs with respect to the neutral axis of the structure so that the airfoil can move either upwards or downwards. This example shows that special attention should be given to the design of the morphing architecture so that the controlled configuration can meet the specified requirements efficiently.

As the number of SMA actuators and the degrees of freedom of the structure increase, so does the complexity of the design problem. The design procedure should also respect: (a) the geometric and structural constraints posed by the controlled structure, and (b) the external loading specifications imposed. For a target morphed shape, the design process should predict the operational temperatures and the positioning of the actuators, while the operational (i.e. power supply) and material costs should be also taken into consideration. The solution of the design problem discussed here requires the accurate prediction of the structural response under the control of SMAs which is then coupled to an optimization tool in order to find the design that best produces the desired shape.

#### 3.1. Structure SMA interaction

The SMA actuators are introduced in a FE structural model using an in house solver, known as NonLinear Builds (NLB) code [29].



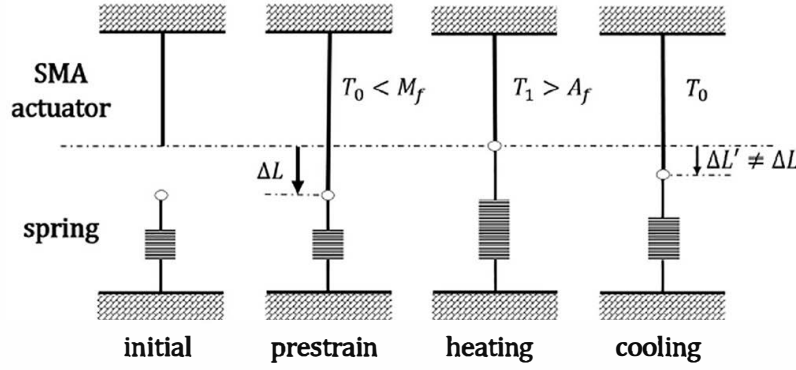


Fig. 2. SMA working principle.

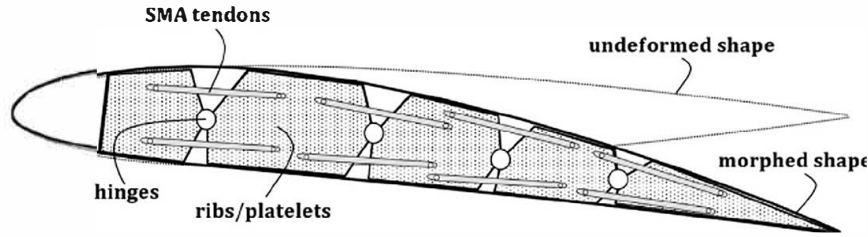


Fig. 3. Airfoil architecture equipped with SMA actuators. Placement of hinges and pairs of SMA "tendons" in order to maximize deformability and to efficiently adjust the shape.

Since aeronautical configurations often have complicated geometries with various structural parts to be modeled, the methodology is developed in a FE analysis framework. This allows to consider the rigidity of the structure, the boundary conditions and the non conservative aerodynamic loading conditions in a consistent manner. The modelling of the thermomechanical behavior of the SMA actuators is based on the model of Brinson.

The solution is based on an iterative algorithm that determines, for a given temperature history and initial conditions, the displacement of the structure and the stresses developed in the SMA actuators. The stresses in the SMA actuators are induced by the temperature variation and are calculated with the aid of the constitutive material law. The structure "sees" the SMA actuators as equivalent, "external", forces equal to the SMA axial force. The other forces acting on the structure influence the SMA thermomechanical behavior and as a result the "external" forces are adjusted anew. This procedure is repeated until the displacement compatibility between the structure and the actuators is imposed and the equilibrium is identified.

Initially the FE model of the structure is created and the nodes to which the SMA actuators are connected are defined. Every SMA actuator is introduced in the FE model as tension only truss elements (denoted as  $m = 1, 2, \dots$ ). The NLB algorithm is outlined step by step below:

#### Initialization of the problem

- For every SMA truss element  $m$ : the actuator's axial strain  $\epsilon_{str}^m$ , calculated from the nodal displacements of the structure, is defined. A second SMA strain  $\epsilon_{SMA}^m$  is calculated from the constitutive relationship (see Section 2) for every SMA actuator.
- For every SMA truss element  $m$ : the initial state parameter  $\xi_{s0}^m, \xi_{T0}^m$ , the length  $L_0^m$  and the temperature  $T_0^m$  are derived from the stress/strain conditions that are applied at the prestress phase.

- For every SMA truss element  $m$ : a starting length  $L_{SMA,0}^m$  is defined corresponding to the initial phase for which no pre strain has been imposed. This length  $L_{SMA,0}^m$  differs from  $L_0^m$  which is the initial element length after it is mounted on the structure.

#### $i^{th}$ pseudo time step (temperature increment $\Delta T_i^m$ ):

Thermal loading is applied at discrete pseudo time intervals, while for every temperature increment, iterations between the structure and the SMA actuator are performed. Within these iterations, the previous and the current configuration are denoted as "old" and "new", respectively. For the  $m^{th}$  SMA actuator the thermal load  $q^m = \Theta(T_i^m - T_0^m)$  is applied, which may differ for each actuator. Subsequently, at the beginning of the increment, the stress  $\sigma_i^{m,old}$  is set equal to the stress of the previous time step  $\sigma_{i-1}^{m,new}$ . The iterative procedure adopted for the current increment follows:

- The state variables  $\xi_s^m, \xi_T^m, \xi^m$  are calculated from the phase changing model.
- The strains  $\epsilon_{SMA}^m$  are derived from  $\xi_s^m, \sigma_i^{m,old}$  and the thermal load  $q^m$ .
- The axial force  $F^m = \sigma_i^{m,old} A_{SMA}^m$  is calculated, where  $A_{SMA}^m$  is the cross section area of every actuator.
- $F^m$  is transformed from the local SMA coordinate system to the global system and the equivalent nodal forces of the structure are calculated. The nodal displacements are obtained with a FE analysis applying the equivalent nodal forces.
- From the updated displacements of the common nodes, the new effective length  $L_{SMA}^{m,new}$  is calculated for every SMA actuator.
- The strain  $\epsilon_{str}^m$  is updated for the  $m^{th}$  SMA actuator from:

$$\epsilon_{str}^m = (L_{SMA}^{m,new} - L_{SMA,0}^m) / L_{SMA,0}^m \quad (4)$$

- The stresses of the  $m^{th}$  SMA actuator are updated as:

$$\sigma_i^{m,new} = \sigma_i^{m,old} + (\epsilon_{SMA}^m - \epsilon_{str}^m) \frac{\partial \sigma}{\partial \epsilon} \bigg|_{T_i}^m \quad (5)$$

where the derivative  $\frac{\partial \sigma}{\partial \epsilon} \big|_{T_i}^m$  is calculated from the constitutive law and the transformation equations, for given temperature  $T_i^m$  and stress  $\sigma_i^{m,old}$ . Note that if  $\sigma_i^{m,new} < 0$ , we set  $\sigma_i^{m,new} = 0$ , since the actuators are tension only.

- The stress values are updated and the error of every actuator is calculated as:

$$e^m \approx |\epsilon_{SMA}^m - \epsilon_{str}^m| / \epsilon_{SMA}^m \quad (6)$$

The total error is:

$$e^{tot} = \sum_m e^m \quad (7)$$

After convergence is achieved, i.e.  $e^{tot} \leq \text{tolerance}$ , the solver proceeds to the next temperature increment.

### 3.2. Design of an optimized morphed configuration

The analysis algorithm is coupled with an optimization solver in order to design aeronautical configurations. The optimization procedure is used to calculate the structural and/or the operational parameters required to design a controlled configuration that is able to achieve pre defined target shapes efficiently. In the present work, the code adopts a stochastic optimization algorithm, suitable for nonlinear structural optimization problems with a modest number of design parameters. The formulation of the optimization problem depends on the problem at hand and it requires to define: (i) the objective function, (ii) the design variables, and (iii) the constraint functions. The optimization problem is expressed in a standard mathematical form as:

$$\begin{aligned} &\text{minimize : } F_{obj}(\mathbf{b}) \\ &\text{subject to : } g_j(\mathbf{b}), j = 1, \dots, m \\ &\text{with : } b_i \in R^i, i = 1, \dots, n \end{aligned} \quad (8)$$

where  $b_i, i = 1, \dots, n$  are the design variables that receive values from the set  $R^i$ , whereas  $F_{obj}(\mathbf{b})$  and  $g_j(\mathbf{b})$  are the objective and constraint functions, respectively. The optimization based design procedure determines the structure that optimally satisfies the problem objectives, which, for shape control problems, is to obtain a target aerodynamic shape. Therefore, the objective function is the error between the target shape geometry  $\mathbf{x}_{tar}$  and the deformed shape of the controlled configuration  $\mathbf{x}_{str}$ , i.e.  $F_{obj} = \|\mathbf{x}_{str}(\mathbf{b}) - \mathbf{x}_{tar}\| / \|\mathbf{x}_{tar}\|$ . The vector of design variables  $\mathbf{b}$  includes the geometric parameters and the final temperature in each SMA actuator. The geometric parameters define the position and the orientation of the SMA actuators. Furthermore, the design problem is constrained by geometric (e.g. available space) limitations and working limitations posed by the actuators, such as the maximum temperature that can be achieved, available power supply, fatigue requirements, etc. The constraints are case dependent and rely on the morphing application examined.

The article discusses single target shape problems. However, in order to design efficient actuation systems, more objectives can be included in the objective function as a weighted sum:

$$F_{obj} = w_1 F_1 + w_2 F_2 + \dots + w_m F_m \quad (9)$$

where  $F_i, i = 1, \dots, m$  are the different problem objectives and  $w_i$  are the corresponding weight coefficients. For example, in order to design a minimum weight actuation system, the  $F_{obj}$  relates the size and the material properties of the actuators to the weight of the actuation system. In this case, the dimensions (e.g. length, diame-

ter) and the material properties (e.g. alloy types, density) of the SMA actuators are also design variables of the optimization problem. If the target is an actuation system with minimum electric energy consumption, a cost function that relates the actuation temperature to the power consumption is added. The latter case is also examined in the present article. It should be noted that the weighted sum of Eq. 9 is a simple approach to handle multiple objective problems [30] and it does not guarantee that the weights assumed will hold for the optimal design as well. A multi objective solver could be alternatively employed for this purpose, but this investigation is beyond the scope of the present study.

## 4. Shape control and design examples

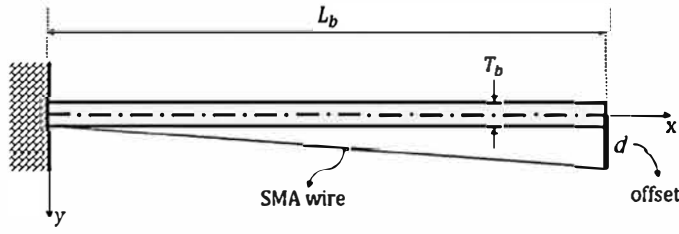
The proposed methodology is evaluated for three numerical studies. The flexible structures considered are geometrically nonlinear, and hence the methodology is developed within a nonlinear FE analysis framework that allows to capture the significantly higher stresses compared to the linear case. The beam element implemented follows the corotational formulation of Crisfield [31]. The code has the capacity to solve for non conservative nodal forces and distributed loads, known as *following force* problems [32].

### 4.1. Cantilever shape control

A cantilever example, initially presented in [5], is adopted here in order to demonstrate the proposed method for coupled SMA structure problems. The configuration examined is equipped with a single SMA actuator (Fig. 4). The cantilever with  $E = 69$  GPa has length  $L_b = 300$  mm and is connected at its free end with the actuator with a small offset  $d$ . In this example, the offset distance used is 5 mm. A rectangular cross section is assumed for the beam with thickness  $T_b = 2$  mm and width  $W_b = 100$  mm. The SMA actuator has diameter  $D_{SMA} = 1.3$  mm and is initially prestrained with strain  $\epsilon_0 = 3\%$  and stress  $\sigma_0 = 0$ , resulting to  $\xi_{s0} = \epsilon_0 / \epsilon_L = 0.45$  for  $\epsilon_L = 6.7\%$ . The material properties assumed for the SMA are shown in Fig. 4.

When the SMA actuator is subjected to a temperature variation, its length changes imposing a force that deforms the cantilever. The force due to the actuation is a follower load since its direction follows the deformation of the cantilever. The term *follower load* refers to non conservative forces that “follow” the deformation of the structure, e.g. the aerodynamic pressure is always perpendicular to the structure. This is an important aspect for structures that undergo large displacements as in the case of morphing structures. The simulation of follower forces is based on the work of Argyris et al. [32,33], who proposed a pertinent correction of the tangent stiffness matrix. The resulting non symmetric stiffness matrix increases the computational cost, while it stabilizes the solution and assures convergence. The cases of both concentrated and distributed non conservative loading have been considered and are included in Appendix A.

A full heating cooling cycle for the SMA actuator is considered. The temperature of the actuator starts from 20 °C, then linearly increases up to 80 °C and it is cooled back to 20 °C. Fig. 5a shows the deformation of the cantilever due to the temperature variation of the SMA actuator. Fig. 5b presents the stress strain equilibrium points for the SMA actuator for different temperature values. As the temperature increases, the pre strained SMA actuator recovers its initial strain  $\epsilon_0$ . As it retracts, the actuator deforms the cantilever and high levels of stress are produced. At the end of the heating phase, the prestrain is almost recovered and only a small residual strain  $\epsilon_r$  remains (Fig. 5b). The predicted *working points* are shown with filled circular markers and determine the working range of the controlled configuration. The working points are iden-



$$\begin{aligned}
 M_{s|f} &= 18.4|9^\circ\text{C} & A_{s|f} &= 34.5|49^\circ\text{C} \\
 E_M &= 26.3\text{GPa} & E_A &= 67\text{GPa} \\
 C_M &= 8\text{MPa}/^\circ\text{C} & C_A &= 13.8\text{MPa}/^\circ\text{C} \\
 \Theta &= 0.55\text{MPa}/^\circ\text{C} & \sigma_{s|f}^{cr} &= 100|170\text{MPa}
 \end{aligned}$$

Fig. 4. Elastic beam controlled with an SMA wire (left) and SMA properties [5] used in this example (right).

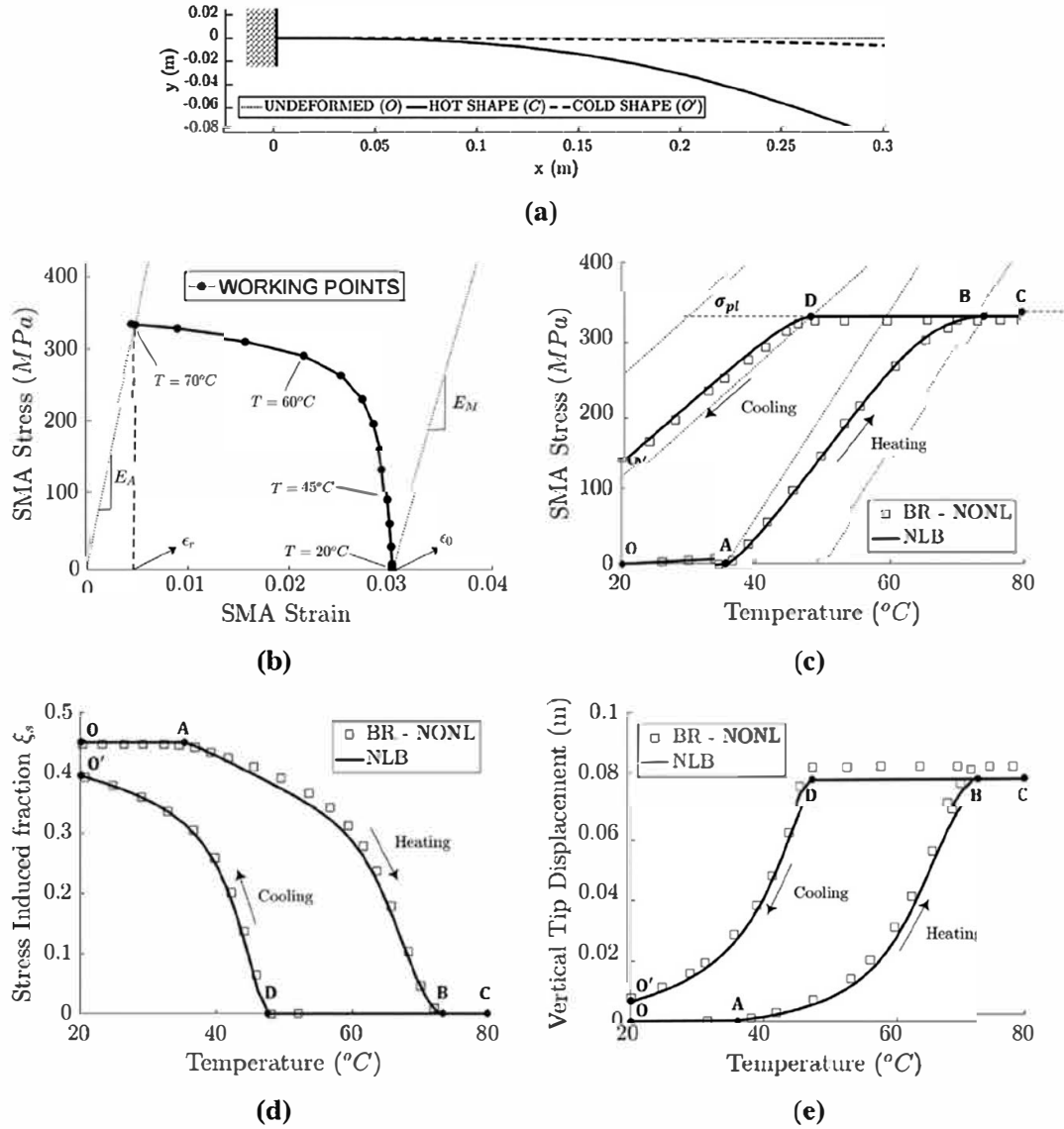


Fig. 5. Cantilever controlled by an SMA actuator: (a) cantilever deformation after heating (HOT SHAPE) and cooling (COLD SHAPE), (b) stress-strain diagram for the SMA wire, (c) stress history and (d) history of stress-induced martensite fraction of the SMA wire with temperature, and (e) end-point vertical deflection of the cantilever with temperature. The proposed methodology (NLB) is compared with numerical results (BR-NONL) from [5].

tified from the equilibrium between: (a) the reaction forces induced from the cantilever to the SMA, and (b) the stress strain temperature state of the actuator; they are contained within the working limits of the actuators which are shown in Fig. 5b with dotted lines.

The results obtained are shown in Fig. 5c while the results of reference [5] are also shown with a hollow square marker. The

heating and cooling procedures are marked as OC and CO', respectively. Fig. 5c presents the stress developed due to the SMA structure interaction as function of the temperature. During heating (OC), the material undergoes an austenitic transformation that starts at  $T \approx 35^\circ\text{C}$  (point A) and is concluded at  $T \approx 70^\circ\text{C}$  (point B). At this temperature, zero martensitic fraction remains as shown in Fig. 5d where the variation of stress induced fraction  $\xi_s$  is pre



sented as function of the temperature. For  $70^\circ\text{C} < T < 80^\circ\text{C}$  (BC), no further transformation takes place and the stress reaches a plateau  $\sigma_{pl} \approx 330$  MPa. As a result, the controlled beam reaches its maximum displacement as presented in Fig. 5a (marked as “HOT SHAPE”), and Fig. 5e where the end point vertical deflection of the cantilever is shown as function of the temperature.

During cooling (CO), the displacement is reversed as shown in Fig. 5. Initially, as the temperature reduces (CD), the actuator and the structure remain at an equilibrium under stress  $\sigma_{pl}$ . At  $T \approx 43^\circ$  (point D), martensitic fraction is generated as the structure recovers its undeformed shape and “pulls” the actuator with it. The martensitic fraction  $\xi_s$  increases with the reduction of temperature (Fig. 5d), while the stress (Fig. 5c) and the beam’s deformation (Fig. 5e) decrease. At  $T = 20^\circ\text{C}$ , the whole configuration reaches a new equilibrium state  $O'$  (“COLD SHAPE” in Fig. 5a) where the whole system balances under a residual stress and a lower martensitic fraction compared to the initial undeformed state  $O$ . Overall, the hysteretic behavior of the SMA actuator is well captured by the NLB code and the methodology produces results in very good agreement with the reference [5].

#### 4.2. Optimal shape control

The next case study shows the capabilities of the proposed design procedure. The NLB code is coupled with an optimization algorithm as discussed in Section 3.2, and is employed for the design of a controlled configuration that is able to achieve a target shape by adjusting the temperature of the SMA actuators. The Covariance Matrix Adaptation Evolution Strategy (CMA-ES) algorithm [34] is adopted for the solution of the optimization problem. Evolutionary algorithms, such as CMA-ES, are appropriate for strongly nonlinear optimization problems where the number of design variables is moderate. In Evolution Strategies (ES), the new solutions (candidates) are selected according to a multivariate normal distribution; recombination procedures and mutations are carried out to produce a new distribution with a different mean value. In the combined CMA-ES approach, the CMA method updates the covariance matrix which represents the *pair wise dependencies* between the variables of this distribution.

The controlled configuration analysed in this study is shown in Fig. 6a. The structure is pinned at its left side, while the right end is free to move vertically. For numerical stability purposes, a low stiffness spring ( $k_{spr} = 1000$  N/m) has been inserted at the free end. The properties of the beam are:  $E = 69$  GPa,  $L_b = 300$  mm,  $T_b = 2$  mm and  $W_b = 100$  mm. The target shape is shown in Fig. 6a; it is produced by a third order polynomial function in order to obtain a realistic convex aerodynamic shape. The controlled beam will obtain the target shape by adjusting the temperature

of the four SMA actuators, shown in Fig. 6b. The optimization procedure will determine the temperature and the position of every actuator.

For this example, the number of SMA actuators is kept constant (here four). Two actuators are placed below the cantilever and two above (Fig. 6b). The SMA actuators are pinned on their left side ( $x = 0$ ) at a fixed vertical distance  $y_{d,m}$  from the neutral axis of the frame. For the problem examined,  $y_{d1,3} = y_{d2,4} = L_b/8$ . The actuators are attached to the structure with the same fixed offset distance  $d = 5$  mm. All SMA actuators are assumed to have a constant diameter  $D_{SMA} = 1$  mm and the same material properties, shown in Table 1. The actuators start from a fully martensitic state ( $\xi_{s0} = 1$ ) at  $T_0 = 20^\circ\text{C}$  and a stress induced fraction  $\xi_{s0} = \epsilon_0/\epsilon_L = 0.66$ , with  $\epsilon_L = 6.1\%$  and  $\epsilon_0 = 4\%$ .

The objective function is the normalized norm of the distance of each point of the beam structure from the target shape, i.e.:

$$F_{obj} = \frac{\|\mathbf{x}_{str} - \mathbf{x}_{tar}\|_2}{\|\mathbf{x}_{tar}\|_2} \quad (10)$$

where  $\mathbf{x}_{str} = (x_{str}, y_{str})$  is the vector containing all the nodal coordinates for the deformed configuration and  $\mathbf{x}_{tar} = (x_{tar}, y_{tar})$  defines the target geometry. The design variables of the optimization process are: (a) the actuation temperature  $T_m$  for each SMA wire with  $m = 1, \dots, 4$ , and (b) the beam node  $N_m$  at which each SMA wire should be attached, with  $m = 1, \dots, 4$ . The bounds for the design variables are:  $T_m \in [40^\circ\text{C}, 250^\circ\text{C}]$  and  $N_m \in [2, N_p]$ , where  $N_p$  is the total number of FE nodes which is fixed in each example;  $N_m$  only admits integer values. All the calculations were carried out for a population size of 10 for each generation. The population size is relatively small in order to attain fast convergence. The optimization process is terminated when the cost function does not improve over 10 consecutive generations by more than  $10^{-6}$ .

Four optimization runs are selectively presented here. For the convex aerodynamic target shape (Fig. 6a), the controlled configuration is tested assuming 16 nonlinear beam elements ( $NLB_{16}$ ) along the structure. An additional calculation for 32 nonlinear beam elements ( $NLB_{32}$ ) is carried out in order to evaluate the sensitivity of the prediction to the FE mesh size. A linear FE formulation for the structure is also examined assuming 16 elements ( $LIN_{16}$ ) in order to investigate the effect of geometric nonlinearity on the optimal design. The results of the optimization procedure are summarized in Table 2. The normalized attachment positions

**Table 1**  
SMA properties for the optimization problem.

$M_s$	48.4 °C	$A_s$	68 °C	$E_M$	20 GPa	$C_M$	6.32 MPa/°C	$\sigma_{sif}^{cr}$	25/78 MPa
$M_f$	43.9 °C	$A_f$	73.8 °C	$E_A$	31.5 GPa	$C_A$	6.73 MPa/°C	$\theta$	0.5 MPa/°C

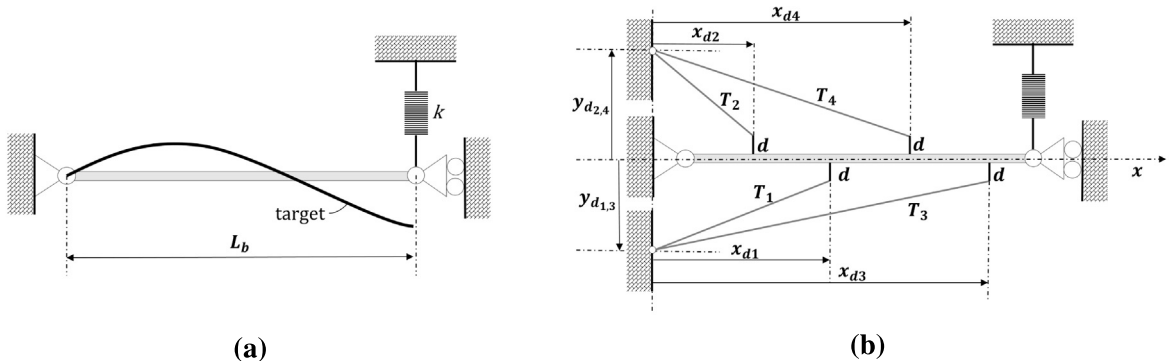


**Fig. 6.** Problem definition for the optimization procedure: (a) controlled configuration and target shape, and (b) the design parameters assumed in this example.

**Table 2**

Optimization results. Initial conditions for the actuators:  $\xi_{s0} = 0.66$  and  $T_0 = 20^\circ\text{C}$ .

NoSMA	1	2	3	4	1	2	3	4
Case	$LIN_{16}$				$NLB_{16}$			
$T$ ( $^\circ\text{C}$ )	211	250	234	229	67	102	136	89
$x_d/L_b$ (%)	93.8	62.5	100	37.5	100	62.5	93.8	37.5
$\xi_s$	0	0	0	0	0.66	0.48	0.37	0.45
Case	$NLB_{32}$				$NLB_{16M}$			
$T$ ( $^\circ\text{C}$ )	50	140	178	86	81	144	107	132
$x_d/L_b$ (%)	62.5	59.4	96.9	31.3	31.3	56.3	56.3	93.8
$\xi_s$	0.68	0.33	0.23	0.44	0.46	0.43	0.44	0.38

$x_{dm}/L_b$  and the actuation temperature  $T_m$  are shown for every actuator.

The deformed shapes produced by the optimized configurations are shown in Fig. 7a together with the target shape which is well captured in every case. The  $NLB_{32}$  gives a slight upward deformation on the second half of the frame. As shown in Table 2,  $LIN_{16}$  and  $NLB_{16}$  predict the same optimal attachment points. However, the temperature prediction is significantly different. The actuation temperatures in  $LIN_{16}$  are higher since larger stresses are required in order to obtain the same deformation. This affects the state of the actuator and highlights the importance of the nonlinear effects in the design process. Furthermore, with the  $NLB_{16}$ , the first actuator (SMA 1) placed below the structure receives zero stress

( $\xi_s = 0.66$ ) due to its temperature and positioning, and does not contribute to the shape control. In the  $NLB_{32}$ , similar attachment positions are identified, showing that the positioning assumed with 16 elements was adequate. SMA 1 is not actuated but receives a small amount of stress that produces a slightly higher stress induced martensitic fraction. In both  $NLB_{16}$  and  $NLB_{32}$ , none of the actuators went through a complete austenitic transformation ( $\xi_s > 0$ ) indicating that the cantilever is capable of achieving even higher deformations. The differences between the  $NLB_{16}$  and  $NLB_{32}$  solutions lead also to variations in the actuation temperatures predicted by the optimization algorithm (Table 2). The mirrored (concave) aerodynamic target shape, with respect to the neutral frame axis ( $x$  axis, see Fig. 7b), is also examined. For the concave shape, the controlled configuration is tested using 16 elements ( $NLB_{16M}$ ). The  $NLB_{16M}$  case provided a positioning that was almost symmetric to  $NLB_{32}$  as shown in Table 2 and Fig. 7b. The target shape is well captured, while contrary to the previous studies, all the actuators are stressed ( $\xi_s < \xi_{s0}$ ) and contribute to the shape control actuation.

In order to investigate the sensitivity of the optimization algorithm to the population size, two more tests were carried out with increased population size for the  $NLB_{16}$  optimization run. The results are shown in Table 3 and in Fig. 7c where the different runs are denoted as "PS10", "PS15" and "PS20" for 10 (i.e. the initial run), 15 and 20 individuals respectively. It can be seen (Fig. 7c) that all three designs capture the target shape sufficiently well and all three have close characteristics (Table 3). SMA 2 is placed close but always after the middle of the cantilever, SMA 3 is at the same position close to the tip, and, finally, SMA 4 is attached on the first

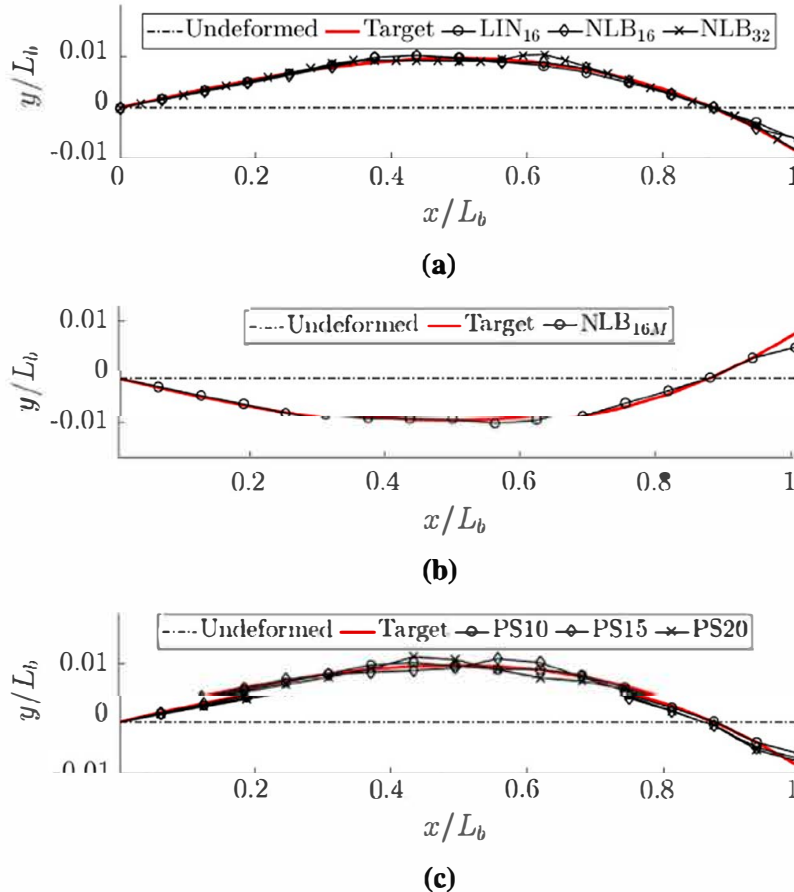


Fig. 7. Deformed controlled shape: (a) the convex aerodynamic target shape, (b) the concave aerodynamic target shape, and (c) sensitivity analysis with 10 (PS10), 15 (PS15) and 20 (PS20) individuals.

Table 3  
NLB<sub>16</sub> sensitivity to the population size.

NoSMA	1	2	3	4	1	2	3	4	1	2	3	4
Pop. Size	10				15				20			
$T$ (°C)	67	102	136	89	76	137	156	78	74	108	169	121
$x_d/L_b$ (%)	100	62.5	93.8	37.5	62.5	56.3	93.8	25.0	50.0	68.8	93.8	43.8

half of the cantilever. The results suggest that the placement of these three SMA actuators are independent variables and they show relatively small sensitivity to the population size for the grid examined (16 elements). On the other hand, the sets of temperature predicted in each case vary significantly, showing a strong dependency on the placement of the actuators. Even small variations of the positions can have a large effect on the temperature calculation. This suggests, however, that for a specific placement of the actuators only one "optimal" set of actuation temperatures exists. Finally, in all three designs, both the temperature and the position of SMA 1 depend on the  $(x_d/L_b, T)$  pairs predicted for the remaining three actuators. This was expected since the target shape could be achieved in this specific application using only three SMA actuators as the analysis demonstrated.

## 5. SMA control of a morphing wing

The last case study examines the application of the proposed algorithm for the shape control of a Morphing Wing Prototype (MWP). The MWP (Fig. 8) is a hybrid electroactive morphing wing, equipped with an SMA based camber control system and trailing edge actuators. Information regarding the construction and the aerodynamic performance of the MWP can be found in [35,20,36]. The range of deformation of the MWP has been studied numerically and experimentally in laboratory conditions in [37], providing the authors of the present article with "reference" downward and upward deflections of the structure. NLB is used first to solve the structure SMA interaction problem for the shape control of the MWP and the results are compared with these investigations

on the constructed prototype (Fig. 8a). Subsequently, the proposed algorithm is adopted in order to optimize the actuation system of the wing. The aim is to produce a morphing wing that achieves a pre described displacement while consuming minimum energy, i.e. with minimum actuation temperature.

The baseline airfoil of the MWP is that of an AIRBUS wing, with a chord  $c_w$  700 mm and a span  $S_w$  590 mm. The camber control system employs SMA actuators inserted on the rear 30% of the chord (Fig. 8c) which is the deformable part of the wing. Eighteen equidistant pairs of SMA actuators cover the whole span of the wing, acting both on the suction (upper) and on the pressure (lower) side of the wing. The actuators are pinned on their left side to the fixed (non deformable) part of the wing and are attached with an offset on the upper and the lower skin side. When the top actuators are heated, the wing is cambered downwards and vice versa, when the bottom actuators of the wing are instead heated. Through this "agonist antagonist" configuration, the wing is able to move efficiently both upwards and downwards and to recover quickly its initial/neutral shape. A rigid body part is attached on the suction side in the trailing edge region of the wing (Fig. 8c). When the upper skin deforms downwards due to the actuation, the attached rigid body comes into contact with the pressure side and slides over the lower skin imposing the downward deformation. The reverse process takes place when the lower part of the wing is instead actuated.

A two dimensional FE model (Fig. 9) is developed for the deformable part of the wing. The model represents one of the 18 equidistant sections, while elastic beam elements were chosen to represent this narrow aluminum ( $E$  69 GPa) skin region. The

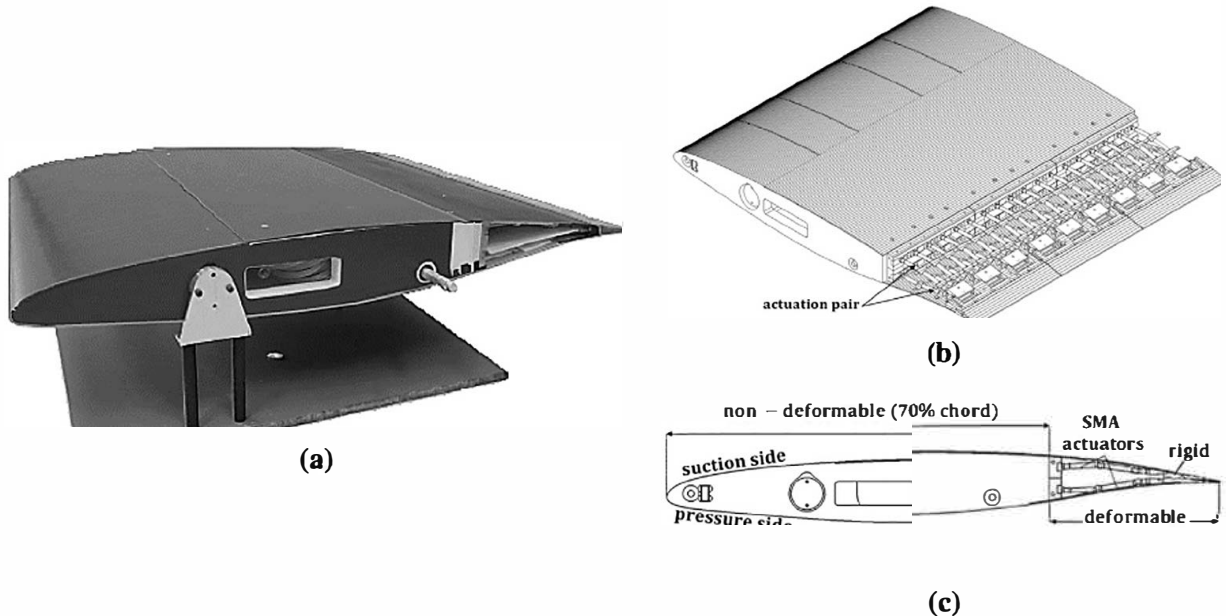


Fig. 8. The Morphing Wing Prototype (MWP): (a) photograph of the electroactive hybrid MWP, (b) 3D CAD schematic with the upper skin removed on the deformable part to reveal the SMA-based actuation, and (c) wing cross-section with one of the 18 actuation pairs on the deformable part of the wing.

beam elements of the skin have thickness  $T_b = 1.5$  mm and width  $W_b = S_w/18 = 32.8$  mm. For the suction and the pressure side of the wing, 30 and 34 beam finite elements have been assumed, respectively. SMA wires made of Nickel Titanium (Ni Ti) alloys with diameter  $D_{SMA} = 1$  mm were mounted on the MWP; the material constants are shown in Fig. 9. The SMAs initially are fully in martensitic phase with  $\xi_{s0} = \epsilon_0/\epsilon_L \approx 45\%$ , where  $\epsilon_0 = 3\%$  is the prestrain and  $\epsilon_L = 6.7\%$ . The two actuators are pinned on their left side and are attached to the wing at three points with an offset (Figs. 8c and 9). The attachments are modeled as pulley/wire type joints that “pull” the respective surface as the wire is tightened. For the transmission of the force between the two sides through the rigid body placed close to the trailing edge of the air foil, the *rigid body/skin* contact problem is considered based on the work of Zavarise et al. [38].

### 5.1. Shape control with the existing actuation system

The structure SMA interaction problem for the shape control of the MWP is first studied. Two cases are examined, heating the upper and then heating the lower actuator, separately. In both cases, the temperature is incrementally varied from  $26^\circ\text{C}$  to  $154^\circ\text{C}$  with  $\Delta T_i = 4^\circ\text{C}$ . When one actuator is heated, the other one remains at a constant, ambient, temperature  $T_0 = 26^\circ\text{C}$ . Fig. 10 shows the results for both cases. Fig. 10a presents the stress variation as function of pseudo time for both actuators, when only the upper one is heated. As the temperature increases, the wing deforms downwards and the stress develops on the upper actuator due to its interaction with the structure. The upper SMA actuator undergoes an *austenitic* transformation which is concluded at  $T \approx 122^\circ\text{C}$  for which the stress reaches a plateau. After its complete transformation, the upper actuator cannot recover more length and hence cannot further deform the wing. As the wing is cambered, the actuator connected on the lower side resists to the change of shape and is stretched. As a result, the stress also develops to the bottom actuator from its interaction with the deforming structure. Due to this stress, the material of the lower actuator transforms from *twinned* to *detwinned* martensite. For the fully deformed wing, the stress in the lower actuator also reaches a plateau (Fig. 10a).

Fig. 10c presents the deformed wing at  $T = 118^\circ\text{C}$  for the upper actuator; the “reference” downward deflection of the morphing wing [37] is also shown with dotted lines. For  $T = 118^\circ\text{C}$ , the reference downward shape is reproduced exactly by the simulation. The working point, i.e. the equilibrium between the wing and the actuators for this temperature, is noted in Fig. 10a with a hexagram marker. For this temperature, the working point is close to the stress plateau, attesting that only a small martensitic fraction

remains and the actuator approaches its working limit. This is in good agreement with the range of deformation of the real constructed prototype. The reverse procedure is shown in Fig. 10b and d where the lower actuator is heated and the wing deforms upwards. For the upward movement, large stresses develop at both actuators (Fig. 10b), compared to the downward deformation where smaller forces were required. In this case, the *austenitic* transformation of the lower SMA actuator is completed at a much higher temperature ( $T \approx 150^\circ\text{C}$ ) due to the increased stress/force required. In Fig. 10d, the deformed wing is presented, showing that the reference shape is captured at  $T = 98^\circ\text{C}$  for the lower actuator. For  $T = 98^\circ\text{C}$ , the working point has not reached the stress plateau (Fig. 10b) suggesting that the actuator has a wider working range. However, the stresses in the actuators significantly increase after this temperature and more upward deflection could possibly damage the constructed prototype.

In this section, the numerical prediction of static equilibrium points was examined for the MWP. For the optimization based design process that follows in the next section, the same analysis will be followed. The goal is to identify optimal shapes that can statically sustain the mechanical and/or aerodynamic loading, while the dynamic transition towards the optimal shape is not be explicitly addressed, even though it is also an important aspect. However, experimental investigations carried out at IMFT on the MWP prototype have provided evidence that there is sufficient smoothness within a dynamic loading sequence, i.e. during the transition from one loading case to the other.

### 5.2. Optimum design of the actuation system

The previous section determined the actuation temperatures in order to obtain the reference downward and upward cambered shapes. In this section, it is investigated whether the actuation system can be re designed in order to achieve the same cambered shapes more efficiently. Modifications concerning only the design of the upper actuator are discussed. The actuator and the target shape are shown in Fig. 11. It was previously shown that the existing design of the actuation system is able to produce this deflection at  $T = 118^\circ\text{C}$  for the upper actuator. It will be investigated whether a new design can produce the same deformed shape for a lower actuation temperature  $T_u < 118^\circ\text{C}$ , i.e. reduced energy consumption. The SMA properties of Fig. 9 and the same initial conditions as those of Section 5.1 are assumed.

The target shape is obtained by minimizing the distance of selected “control” points placed on the wing from target positions (Fig. 11b). The control points are used instead of the whole surface in order to facilitate and speed up the convergence of the optimization problem. The error is measured as:

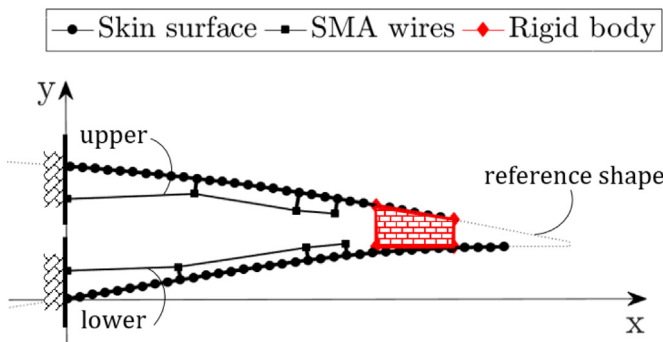
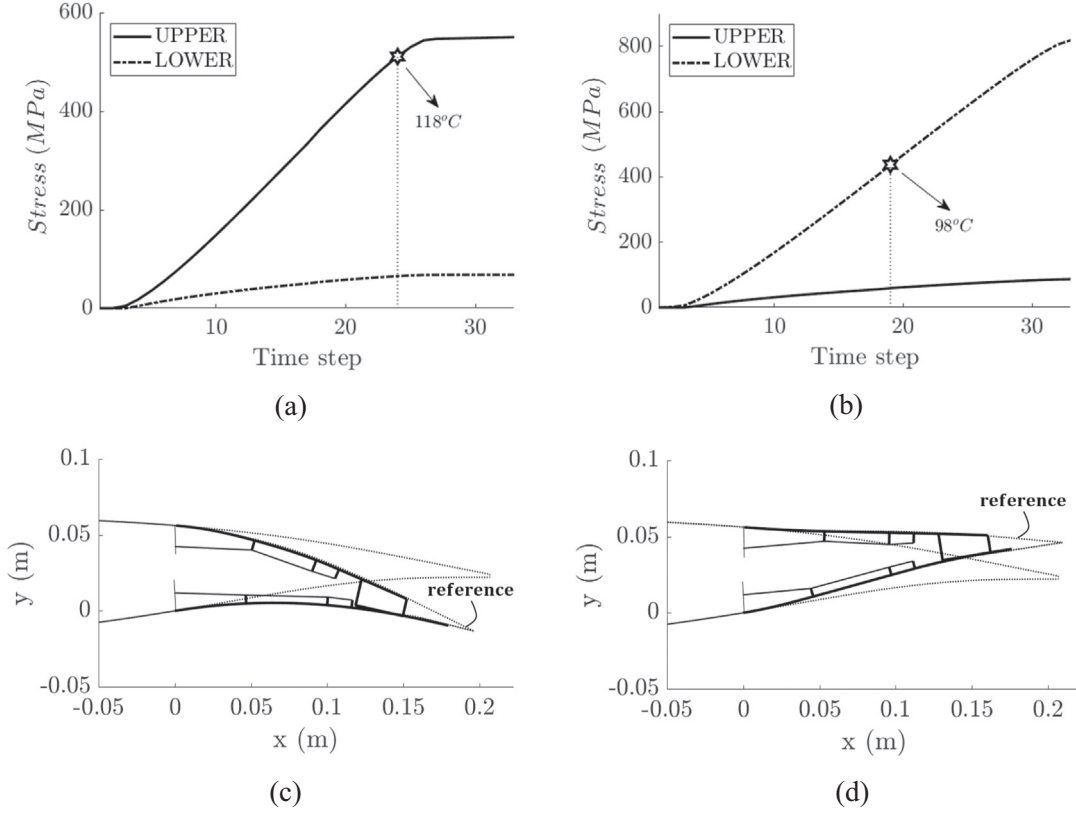
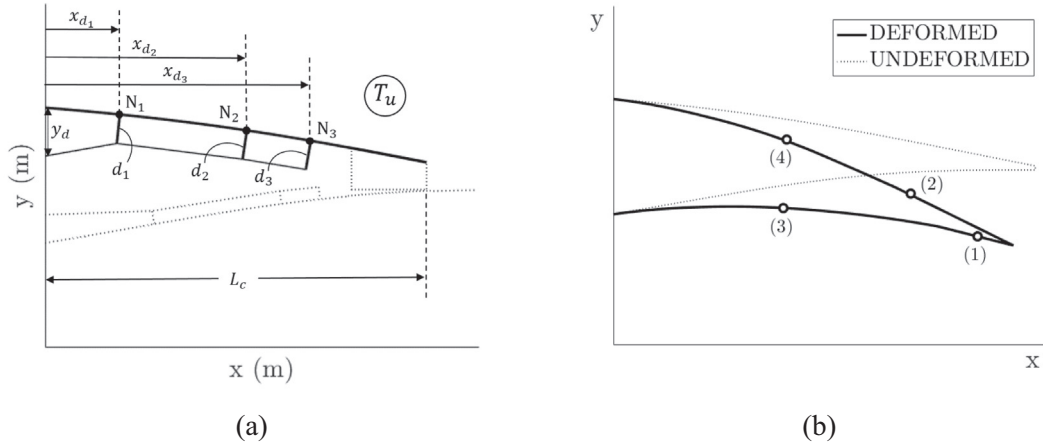


Fig. 9. FE model and boundary conditions (left), and Ni-Ti SMA properties [37] for the actuators of the morphing wing (right).





**Fig. 10.** Aerodynamic shape control of the MWP. Stress variation in both actuators for: (a) downward deflection by heating the upper actuator, and (b) upward deflection by heating the lower actuator. Cambering of the wing: (c) downwards by heating the upper actuator at  $T = 118^\circ\text{C}$ , and (d) upwards by heating the upper actuator at  $T = 98^\circ\text{C}$ .



**Fig. 11.** Revisiting the actuation system of the MWP: (a) design variables for the upper actuator, and (b) target shape and "control" points.

$$F_{dist} = \sum_{k=1}^{n_p} \sqrt{(x_{str}^k - x_{tar}^k)^2 + (y_{str}^k - y_{tar}^k)^2} \quad (11)$$

where  $n_p = 4$  is the number of control points,  $\mathbf{x}_{str}, \mathbf{y}_{str}$  the coordinates of the structural control points and  $\mathbf{x}_{tar}, \mathbf{y}_{tar}$  the target coordinates. The sensitivity of the design to the number of control points used has been evaluated through a parametric study and the four control points were found adequate for capturing the target shape.

In order to identify a new design that can produce the target shape for a reduced temperature, the actuation temperature  $T_u$

has to be taken into account in the objective function. The objective function adopted considers both the error from the target shape and the contribution of the temperature:

$$F_{obj} = F_{dist}/L_c + w_g \cdot \log(10^{T_u/T_{MAX}}) \quad (12)$$

where  $L_c = 0.1589$  m is a characteristic length (see Fig. 11a) used to normalize  $F_{dist}$ , and  $w_g$  a weight parameter that scales the contribution of  $T_u$  to a range comparable to  $F_{dist}/L_c$ . The weight  $w_g$  has been evaluated through numerical investigations on a trial and error basis and its value ranges between  $0.3 \times 10^{-2} \div 0.65 \times 10^{-2}$ . The

design variables included in the optimization process are shown in Fig. 11a. Similar to the existing design of the actuation system, three attachment positions are considered.

Two optimization cases denoted as  $OPT_1$  and  $OPT_2$  are discussed. For the first optimization problem ( $OPT_1$ ), a weight factor  $w_g = 0.5 \cdot 10^{-2}$  is assumed. Besides  $T_u$ , the rest of the design variables are: (a) the points on the wing surface where the three pulley/wire joints are attached, i.e. the  $N_1, N_2, N_3$  beam nodes of the upper skin, (b) the offset distances  $d_1, d_2, d_3$ , and (c) the vertical distance  $y_d$  below the upper skin at which the actuator is pinned. The design temperature ranges between  $[40^\circ\text{C}, 118^\circ\text{C}]$ . The bounds for the three attachment positions are:  $N_i \in [2, 24]$ , where  $N = 24$  is the latest acceptable FE node for the attachment of the actuator. Additional constraints are set for the attachments positions, following Fig. 11a:  $N_1 - N_2 \leq 0, N_2 - N_3 \leq 0$  and  $N_1 - N_3 < 0$ . If  $N_2 \approx N_1$  or  $N_3 \approx N_2$ , the second pulley/wire joint is removed from the simulation (and marked as “merged”). The bounds for  $y_d$  and the offsets are imposed by the geometry of the wing. Specifically, the bounds for the distance between the upper skin and the position where the actuator is pinned, are:  $y_d \in [5\text{mm}, 55\text{mm}]$ . Furthermore, all offset distances are set equal (d) and vary in between 1 mm and 15 mm.

The second optimization problem ( $OPT_2$ ) is carried out for a fixed temperature  $T_u = 110^\circ\text{C}$ . This approach assumes  $w_g = 0$  for the temperature and the optimizer searches only for the geometric design variables  $[N_1, N_2, N_3, y_d, d]$  with  $F_{obj} = F_{dist}/L_c$  (Eq. 12). The same bounds and constraints are adopted for the design parameters, except for the  $T_u$  which is not a design variable for  $OPT_2$ . For  $OPT_1$  a total of 200 generations was carried out for a population size of 9 for each generation. For  $OPT_2$ , 311 generations were evaluated for a population size of 8. The optimization runs are terminated when the cost function does not improve over 10 consecutive iterations by more than  $10^{-6}$ .

The re designed configurations are shown in Fig. 12 at a deformed position and the results are summarized in Table 4. The “original” design (Section 5.1), i.e. the architecture prior to the optimization, is shown with dotted lines (denoted as ORG).  $OPT_1$  (Fig. 12a) captures the target shape at a lower actuation temperature  $T_u = 113^\circ\text{C}$  compared to ORG ( $T_u = 118^\circ\text{C}$ ). The deformed aerodynamic profile has been adequately captured by the optimized configuration, resulting in a low  $F_{dist}$  value (Table 4). The first joint is moved towards the front (Fig. 12a) at  $N_1 = 9$ , to the left of the first ORG attachment. The optimizer predicts that  $N_2 = N_1$  suggesting that these two attachment points could be merged. The third joint is placed at the last acceptable FE node

( $N_3 = 24$ ). The vertical distance  $y_d$  resulting from the optimization process is almost 3 mm larger than that of the reference design, while an increase of approximately 20% of the offset  $d$  is also shown in Table 4. Due to this increased offset, the optimized actuation systems produces the sufficient moment to camber the airfoil at a reduced temperature.

The  $OPT_1$  solution was chosen as the best out of nine independent optimization runs, each starting from a randomly generated initial population. Table 5 shows the statistics for  $OPT_1$ , calculated from this series of optimization runs. The best and worst optimized solutions, along with the mean and the standard deviation ( $std$ ) values for the design variables and the objective function are provided in the table. The best solution provides an  $F_{obj}$  well below the mean value, while the standard deviation for the objective function is around 10% of the mean value. The design variables that present the higher variation are the position of the second attachment point  $x_{d2}$  and the vertical distance  $y_d$ . The second attachment point tends to be merged either with the first or the third attachment point. As a result, the average  $x_{d2}$  value is in the middle, between  $x_{d1}$  and  $x_{d3}$ , and naturally presents the highest variation from all three attachment points. Finally, the vertical distance  $y_d$  seems to play only a secondary role in the design.

Fewer optimization runs were carried out for  $OPT_2$  since the computational cost for such a statistical evaluation was significant. The design produced by  $OPT_2$  is shown in Fig. 12b and the deformed aerodynamic shape is well captured by the optimized configuration. There are a few differences between  $OPT_1$  and  $OPT_2$  designs. The first joint for  $OPT_2$  is placed at  $N_1 = 12$  and the two remaining attachments are moved at the last acceptable node  $N_2 = N_3 = 24$ . The calculation supports the previous observation that only two attachments are sufficient in producing the deformed shape. The predicted vertical distance  $y_d$  is lower than in  $OPT_1$  (Table 4). However, even higher offsets are predicted in  $OPT_2$  so that the design can achieve the downward deformation with the fixed  $T_u = 110^\circ\text{C}$ .

Overall, the  $OPT_2$  design is more energy efficient since it produces the target shape at a lower temperature. This signifies a faster responding actuation system and reduced energy consumption (i.e. “greener” architecture) when multiple SMA actuators are involved. The reduced actuation temperature also suggests that the new actuation system can sustain the target shape under larger aerodynamic loads since the margin from a full austenitic transformation is increased. Furthermore, both proposed architectures are more robust since the optimizer removed a non contributing intermediate joint, producing a less complex actuation architecture that

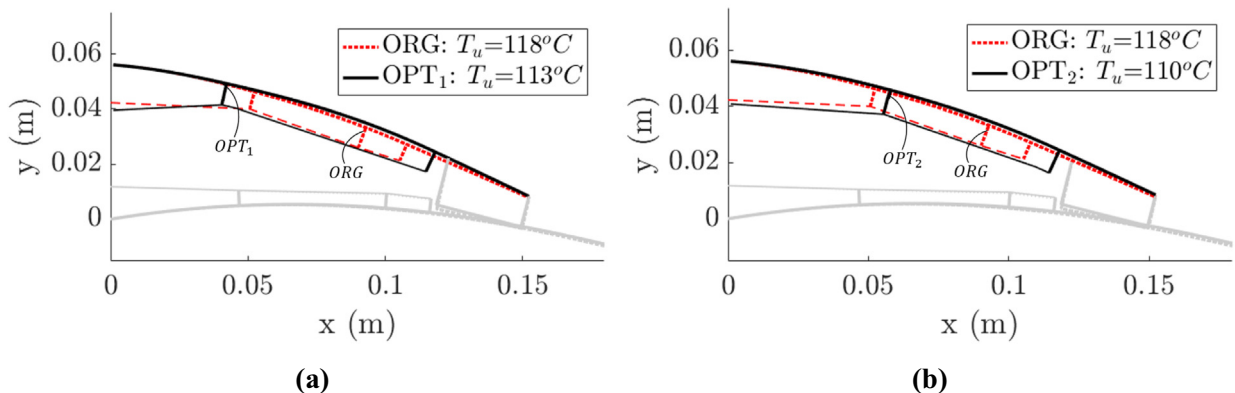


Fig. 12. Comparison of (a)  $OPT_1$  and (b)  $OPT_2$  solutions with the existing actuation system ORG; the optimization arrived at the target shape at different actuation temperatures.

**Table 4**

$OPT_1$  and  $OPT_2$  solutions compared with ORG;  $T_u$  was fixed for  $OPT_2$  to 110 °C.

Case	$T_u$ (°C)	$x_{d1}/L_c$	$x_{d2}/L_c$	$x_{d3}/L_c$	$y_d$ (mm)	$d$ (mm)	$F_{dist}/L_c$
ORG	118	33.4%	60.0%	70.0%	13.8	≈ 6.5	–
$OPT_1$	113	26.8%	merged	76.6%	16.5	7.9	2.2%
$OPT_2$	<b>110</b>	36.7%	merged	76.6%	15.3	8.9	2.6%

**Table 5**

Statistics for  $OPT_1$  solution.

$OPT_1$	$T_u$ (°C)	$x_{d1}$ (mm)	$x_{d2}$ (mm)	$x_{d3}$ (mm)	$y_d$ (mm)	$d$ (mm)	$F_{obj}$
best	113	42.6	47.8	121.8	16.5	7.9	0.0283
worst	111	37.4	53.13	121.8	17.8	6.8	0.0385
mean	114	32.8	81.2	117.7	26.7	8.4	0.0313
std	2.4	12.4	22.1	4.9	13.1	0.7	0.0033

can be easily implemented. Nevertheless, the investigation has shown that the architecture of Jodin [37] was well designed and only slight changes on the placement of the pulley/wire joints are required in order to maximize the efficiency of the actuation system.

Finally, the aerodynamic performance has been evaluated for the  $OPT_2$  optimized profile and has been compared to that of the ORG actuation system. More specifically, low Mach aerodynamic calculations have been carried for the 2D airfoil profiles using the XFOIL [39] solver. The profiles have been investigated for an angle of attack  $\alpha_o = 10^\circ$  and a Reynolds number  $Re = \frac{Uc}{\nu_{air}} = 10^6$ , where  $U$  is the flow velocity,  $c$  is the aerodynamic chord length and  $\nu_{air}$  is the air viscosity. At ambient atmospheric conditions, this flow configuration approaches the take off/landing flight phase where the cambering of the wing is usually evoked. For the ORG design, the aerodynamic lift coefficient is  $c_L = 1.12$  and the drag coefficient of the profile is  $c_D = 0.027$ . This leads to a lift to drag ratio  $L/D = 41.5$  which characterizes the aerodynamic efficiency of the profile. For the  $OPT_2$  optimized profile, the lift coefficient is  $c_L = 1.11$  and the drag coefficient is  $c_D = 0.26$ , resulting to  $L/D = 42.7$ . Therefore, the aerodynamic force components are slightly altered for the optimized case due to the differences between the two shapes (Fig. 12b). Both the lift and the drag coefficients are slightly reduced. However, this leads to an increase of the aerodynamic efficiency showing that the optimized profile has also enhanced aerodynamic performance.

## 6. Conclusions

The shape control of flexible deformable aeronautical structures with SMA actuators was discussed in this paper. The study focused on a fast and robust design procedure for novel SMA based actuation architectures that are optimally controlled. The SMA actuators are introduced in a FE structural model in order to solve the coupled structure SMA problem in the context of a nonlinear FE analysis. The solver determines, for a given temperature history, the displacement of the structure and the stresses developed due to the temperature variation of SMA actuators. The structure is coupled with the SMA actuators through equivalent nodal following forces. The design approach is developed by coupling the FE solver with a stochastic optimization algorithm to solve the constrained shape control problem. The final temperature and the orientation of the SMA actuators with respect to the controlled structure are identified in order to determine configurations able to attain target shapes using SMA actuators.

The method proposed was validated through reference test cases and evaluated on the design of a simplified controlled configuration able to achieve a target aerodynamic shape. The design produced a robust configuration employing less actuators than what was initially assumed. It was also shown that geometric nonlinearities are extremely relevant when designing flexible morphing architectures. Furthermore, the approach was evaluated in the optimization of a real morphing wing. The design methodology was successfully adopted to revisit the architecture of the actuation system in order to consume less energy. The two optimized designs that were proposed by the current investigation were both able to produce the target deformation at a lower actuation temperature and with fewer pulley/wire joints. The methodology presented was proven able to optimize morphing architectures in order to create more robust designs that can potentially sustain the target shape under larger aerodynamic loads.

## Declaration of Competing Interest

The authors declare that they have no known competing financial interests or personal relationships that could have appeared to influence the work reported in this paper.

## Appendix A

A cantilever and a ring beam example under non conservative forces are examined in this Appendix in order to verify the NLB code for geometrically nonlinear problems with follower loads. Follower loads refer to non conservative forces that “follow” the deformation of the structure. The cases of both concentrated (cantilever example) and distributed (ring example) non conservative loading have been considered. The simulation of follower forces is based on the work of Argyris et al. [32,33].

The cantilever (Fig. 13a) of length  $L_b = 100$  mm undergoes large deflection due to a non conservative point force that acts at its free end. A ring (Fig. 14a) of radius  $R = 100$  mm is subjected to an inward pressure that is given by the expression  $p = p_0(1 + \cos 2\theta)$ , where  $p_0$  is the maximum load amplitude and  $\theta$  is the angular coordinate of the ring geometry. Since the ring is doubly symmetric only one quarter is considered. The properties assumed for the two examples are  $E = 210$  GPa,  $I_b = 1.6667 \text{ cm}^4$  and  $A = 20 \text{ cm}^2$ . Ten and eighteen elements were used for the cantilever and for the ring problem, respectively. Figs. 13a and b show the displacement and the load displacement diagrams for the beam example and Fig. 14b presents the deformed structure for one quarter of the ring. These figures show that the NLB code is robust and pro

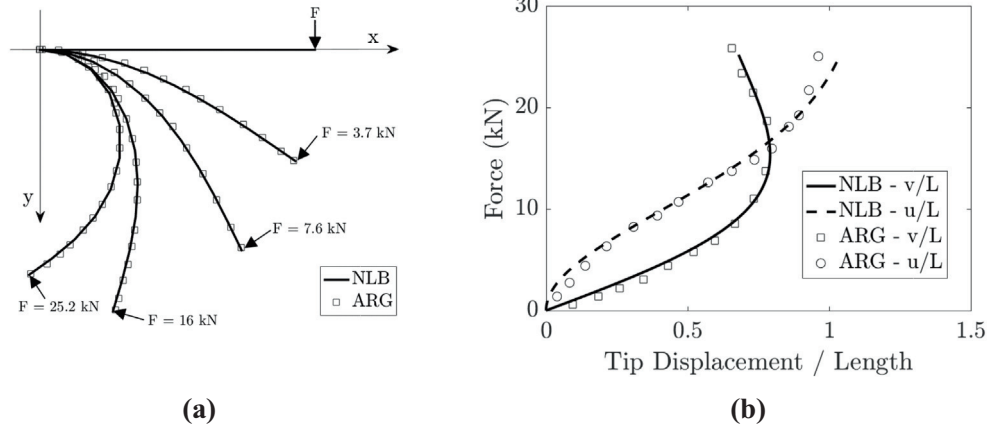


**Fig. 13.** Comparison of the NLB code with numerical results from Argyris et al. [33] (ARG): (a) large deflection of cantilever under non-conservative tip load, and (b) load-displacement diagram of the end point.

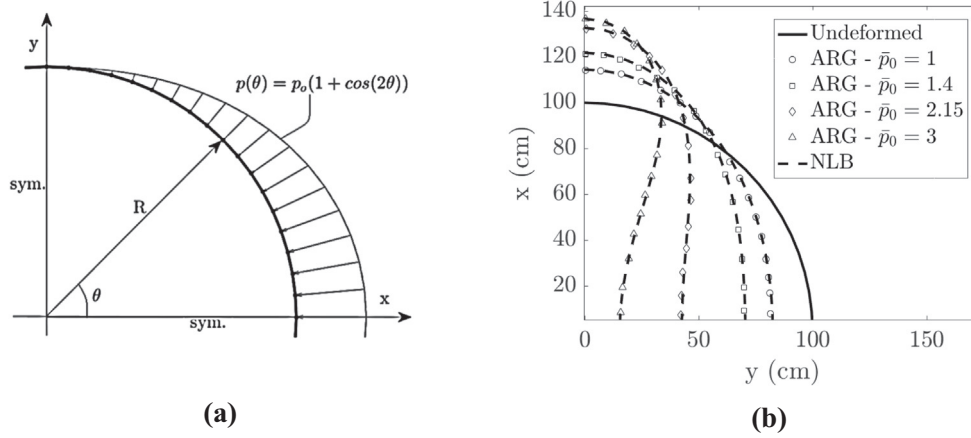


**Fig. 14.** Comparison of the NLB code with Argyris et al. [33] (ARG): (a) 1/4 ring under non-conservative nonuniform normal pressure, and (b) large deflection of circular ring for different load amplitudes  $p_0$ .  $p_0 r^3 / EI$ .

duces results identical to those of Argyris et al. [33] even for large displacements.

## References

- [1] McGowan A-MR, Washburn AE, Horta LG, Bryant RG, Cox DE, Siochi EJ, et al. Recent results from NASA's morphing project. *Smart structures and materials 2002: industrial and commercial applications of smart structures technologies*, vol. 4698. International Society for Optics and Photonics; 2002. p. 97–111.
- [2] Concilio A, Lecce L. Historical background and current scenario. In: Concilio A, Dimino I, Lecce L, Pecora R, editors. *Morphing wing technologies*. Butterworth-Heinemann; 2018. p. 3–84 [chapter 1].
- [3] Barbarino S, Saavedra Flores E, Ajaj RM, Dayyani I, Friswell MI. A review on shape memory alloys with applications to morphing aircraft. *Smart Mater Struct* 2014;23:63001.
- [4] Lecce L, Concilio A, editors. *Shape memory alloy engineering: for aerospace, structural and biomedical applications*. Amsterdam: Butterworth-Heinemann; 2014.
- [5] Brinson LC, Huang MS, Boller C, Brand W. Analysis of controlled beam deflections using SMA wires. *J Intell Mater Syst Struct* 1997;8(1):12–25.
- [6] Shu SG, Lagoudas DC, Hughes D, Wen JT. Modeling of a flexible beam actuated by shape memory alloy wires. *Smart Mater Struct* 1997;6(3):265–77.
- [7] Bandeira EL, Savi MA, Monteiro PCdC, Netto TA. Finite element analysis of shape memory alloy adaptive trusses with geometrical nonlinearities. *Arch Appl Mech* 2006;76(3):133.
- [8] Gao X, Turner TL, Burton D, Brinson LC. Finite element analysis of adaptive-stiffening and shape-control SMA hybrid composites. *Smart structures and materials 2005: active materials: behavior and mechanics*, vol. 5761. International Society for Optics and Photonics; 2005. p. 406–16.
- [9] Barbarino S, Pecora R, Lecce L, Concilio A, Ameduri S, Calvi E. A novel SMA-based concept for airfoil structural morphing. *J Mater Eng Perform* 2009;18(5):696–705.
- [10] Barbarino S, Pecora R, Lecce L, Concilio A, Ameduri S, De Rosa L. Airfoil structural morphing based on SMA actuator series: Numerical and experimental studies. *J Intell Mater Syst Struct* 2011;22(10):987–1004.
- [11] Icardi U, Ferrero L. SMA actuated mechanism for an adaptive wing. *J Aerospace Eng* 2011;24(1):140–3.
- [12] Solomou AG, Machairas TT, Saravanos DA. A coupled thermomechanical beam finite element for the simulation of shape memory alloy actuators. *J Intell Mater Syst Struct* 2014;25(7):890–907.
- [13] Machairas T, Kontogiannis A, Karakalas A, Solomou A, Riziotis V, Saravanos D. Robust fluid-structure interaction analysis of an adaptive airfoil using shape memory alloy actuators. *Smart Mater Struct* 2018;27(10):105035.
- [14] Seelecke S, Müller I. Shape memory alloy actuators in smart structures: Modeling and simulation. *Appl Mech Rev* 2004;57(1):23–46.
- [15] Banerjee A, Bhattacharya B, Mallik AK. Optimum discrete location of Shape Memory Alloy wire for enhanced actuation of a compliant link. *J Mech Des* 2010;132(2). <https://doi.org/10.1115/1.4000643>.
- [16] Ameduri S, Brindisi A, Tiseo B, Concilio A, Pecora R. Optimization and integration of shape memory alloy (SMA)-based elastic actuators within a morphing flap architecture. *J Intell Mater Syst Struct* 2012;23(4):381–96.
- [17] Ghommam M, Hajj MR, Mook DT, Stanford BK, Beran PS, Snyder RD, et al. Global optimization of actively morphing flapping wings. *J Fluids Struct* 2012;33:210–28.
- [18] Smart Morphing & Sensing (SMS) for aeronautical configurations. H2020-EU.3.4 research project. Grant agreement ID: 723402. Coordinator: Institut National Polytechnique de Toulouse (2017–2020). URL [www.smartwing.org/SMS/EU](http://www.smartwing.org/SMS/EU).



- [19] Scheller J, Jodin G, Rizzo KJ, Duhayon E, Rouchon J-F, Triantafyllou MS, et al. A combined smart-materials approach for next-generation airfoils. *Solid State Phenom* 2016;251:106–12.
- [20] Jodin G, Motta V, Scheller J, Duhayon E, Döll C, Rouchon J-F, et al. Dynamics of a hybrid morphing wing with active open loop vibrating trailing edge by time-resolved PIV and force measures. *J Fluids Struct* 2017;74(Supplement C):263–90.
- [21] Birman V. Review of mechanics of Shape Memory Alloy structures. *ASME, Appl Mech Rev* 1997;50(11):629–45.
- [22] Tanaka K, Kobayashi S, Sato Y. Thermomechanics of transformation pseudoelasticity and shape memory effect in alloys. *Int J Plast* 1986;2(1):59–72.
- [23] Liang C, Rogers C. One-dimensional thermomechanical constitutive relations for shape memory materials. *J Intell Mater Syst Struct* 1990;1(2):207–34.
- [24] Brinson L. One-dimensional constitutive behavior of Shape Memory Alloys: Thermomechanical derivation with non-constant material functions and redefined martensite internal variable. *J Intell Mater Syst Struct* 1993;4(2):229–42.
- [25] Auricchio F, Sacco E. A one-dimensional model for superelastic shape-memory alloys with different elastic properties between austenite and martensite. *Int J Non-Linear Mech* 1997;32(6):1101–14.
- [26] Auricchio F, Taylor RL, Lubliner J. Shape-memory alloys: macromodelling and numerical simulations of the superelastic behavior. *Comput Methods Appl Mech Eng* 1997;146(3):281–312.
- [27] Boyd JG, Lagoudas DC. A thermodynamical constitutive model for shape memory materials. Part I. The monolithic shape memory alloy. *Int J Plast* 1996;12(6):805–42.
- [28] Chung J-H, Heo J-S, Lee J-J. Implementation strategy for the dual transformation region in the Brinson SMA constitutive model. *Smart Mater Struct* 2006;16(1):N1–5.
- [29] Simiriotis N. Numerical study and physical analysis of electroactive morphing wings and hydrodynamic profiles at high reynolds number turbulent flows [Phd thesis]. Toulouse: INPT; 2020.
- [30] Yang X-S. Multi-objective optimization. In: Yang X-S, editor. *Nature-inspired optimization algorithms*. Oxford: Elsevier; 2014. p. 197–211 [chapter 14].
- [31] Borst Rd, Crisfield MA, Remmers JC, Verhoosel CV. Geometrically non-linear analysis. In: *Non-linear finite element analysis of solids and structures*. John Wiley & Sons Ltd; 2012. p. 63–111.
- [32] Argyris JH, Dunne PC, Scharpf DW. On large displacement-small strain analysis of structures with rotational degrees of freedom. *Comput Methods Appl Mech Eng* 1978;14(3):401–51.
- [33] Argyris JH, Symeonidis S. Nonlinear finite element analysis of elastic systems under nonconservative loading-natural formulation. part I. Quasistatic problems. *Comput Methods Appl Mech Eng* 1981;26(1):75–123.
- [34] Hansen N. The CMA evolution strategy: A comparing review. In: *Towards a new evolutionary computation. Studies in fuzziness and soft computing*, vol. 192. Berlin, Heidelberg: Springer; 2006. p. 75–102.
- [35] Jodin G, Scheller J, Rizzo KJ, Duhayon E, Rouchon J-F, Braza M. Dimensionnement d'une maquette pour l'investigation du morphing électroactif hybride en soufflerie subsonique. In: 22ème Congrès Français de Mécanique [CFM2015]. AFM, Association Française de Mécanique; 2015. p. 1–13.
- [36] Simiriotis N, Jodin G, Marouf A, Elyakime P, Hoarau Y, Hunt JCR, et al. Morphing of a supercritical wing by means of trailing edge deformation and vibration at high Reynolds numbers: Experimental and numerical investigation. *J Fluids Struct* 2019;91. <https://doi.org/10.1016/j.jfluidstructs.2019.06.016>.
- [37] Jodin G. Hybrid electroactive morphing at real scale - application to Airbus A320 wings [Phd thesis]. Toulouse: INPT; 2017.
- [38] Zavarise G, De Lorenzis L, Taylor RL. A non-consistent start-up procedure for contact problems with large load-steps. *Comput Methods Appl Mech Eng* 2012;205–208:91–109.
- [39] Drela M. XFOIL: An analysis and design system for low reynolds number airfoils. In: *Low Reynolds number aerodynamics*. In: Mueller TJ, editor. *Lecture notes in engineering*, vol. 54. Berlin, Heidelberg: Springer; 1989.